



Cite this: *Mater. Adv.*, 2025,  
6, 3957

## Superior photocatalytic degradation of Reactive Orange 16 by Ag–AgCl/BiOCl nanocomposites under visible light†

Kamya Jasuja<sup>a</sup> and Raj Kumar Das  <sup>ab</sup>

Due to unregulated dumping, the concentration of reactive dyes in wastewater has consistently increased. To mitigate their harmful nature, successful eradication becomes crucial. In this regard, Ag–AgCl–BiOCl nanocomposites were constructed utilizing a simple co-precipitation approach to evaluate the photocatalytic degradation activity towards Reactive Orange 16 in the presence of visible light. The synthesized catalyst was characterized using different methods, including field emission scanning electron microscopy (FESEM), high-resolution transmission electron microscopy (HRTEM), X-ray diffraction (XRD), X-ray photoelectron spectroscopy (XPS), diffuse reflectance spectroscopy (DRS), etc. Furthermore, XPS spectra show the co-existence of Ag(0) and Ag(+1) in the nanocomposite. The loading of Ag–AgCl results in lowering of electron–hole pair recombination and charge transfer resistance. As a result, AB10 outperformed all other nanocomposites in terms of photocatalytic activity, achieving 92% in 90 minutes. The control experiments suggest that holes act as the reactive species in the photocatalytic reactions, whereas electrons, hydroxyl radicals, and superoxide anions do not participate in the degradation process. Remarkably, Bi(III) acts as an electron scavenger to afford Bi(0). Ag(0), as well as the *in situ* generated Bi(0), can play an imperative role in improving the photocatalytic degradation efficiency owing to the localized surface plasmon resonance phenomenon. Furthermore, high-resolution mass spectroscopy (HRMS) confirms the presence of smaller fragments, resulting in a more in-depth understanding of the photocatalytic degradation process. The synthesized catalyst is exceptionally stable and recyclable. As a result, the photocatalyst has the potential to eliminate the reactive dye from wastewater.

Received 7th February 2025,  
Accepted 25th April 2025

DOI: 10.1039/d5ma00105f

[rsc.li/materials-advances](http://rsc.li/materials-advances)

### 1. Introduction

The substantial expansion of the textile sector has led to environmental hazards because of the effluents that include strong concentrations of coloring agents—reactive dyes and other organic and inorganic compounds.<sup>1–4</sup> A chromophore in reactive dyes possesses a substituent that interacts with the substrate to establish a covalent connection during the dyeing process. They possess excellent wet fastness, providing them an edge over other dyes constrained by physical adsorption or mechanical entrapment.<sup>5</sup> Unfortunately, a substantial portion of the dyes does not get attached with the textile during the dyeing process and is discharged directly into the environment.

These dyes are xenobiotic compounds that, besides being carcinogenic and genotoxic, can adversely affect water quality due to their coloration, elevated pH, chemical oxygen demand, and limited biodegradability. These dyes can lead to health complications such as asthma, allergic conjunctivitis, hemorrhages, and central nervous system diseases.<sup>6–10</sup> Even at minimal concentrations (below 1 ppm), these colours adversely affect aquatic ecosystems. Consequently, the elimination of these harmful pollutants from wastewater is imperative and vital. Adsorption coagulation, flocculation, and biological treatments are widely employed methods for the treatment of industrial effluents to eliminate these pigments.<sup>11</sup> Photocatalytic degradation is acknowledged as one of the most efficient techniques for the removal of industrial effluents, as it eradicates them completely instead of merely transferring them from one source to another. Photocatalysis refers to the acceleration of a photoreaction facilitated by a catalyst. The tetragonal matlockite structure of BiOCl is characterized by  $[Bi_2O_2]$  slabs that are interspersed with double halogen slabs. The multilayered structure of BiOX results in inherent static electric

<sup>a</sup> Department of Chemistry and Biochemistry, Thapar Institute of Engineering & Technology, Patiala-147004, Punjab, India. E-mail: rkdas@thapar.edu

<sup>b</sup> TIEET-Virginia Tech Center of Excellence in Emerging Materials, Thapar Institute of Engineering and Technology, Patiala, 147004, India

† Electronic supplementary information (ESI) available. See DOI: <https://doi.org/10.1039/d5ma00105f>



fields, which provide adequate space to generate atom and orbital polarization. Due to its chemical stability, anti-corrosive properties, and nontoxicity, BiOCl functions as an efficient photocatalyst.<sup>12,13</sup> BiOCl possesses a wide band gap. So, it predominantly absorbs in the ultraviolet region. Moreover, the rapid electron-hole pair recombination limits the activity of bare BiOCl as a photocatalyst. Consequently, loading with other metals and nonmetals and constructing heterojunctions with other semiconductors can enhance its reactivity.<sup>14</sup> Nowadays, silver halides have emerged as a new generation of semiconductors due to their various properties, such as high photosensitivity and the ability to absorb visible light, making the material more efficient in degrading the target pollutant.<sup>14,15</sup> Moreover, the synthesis of silver halides often leads to the formation of metallic silver (Ag) *via in situ* reduction. The presence of Ag can be highly beneficial for photocatalytic reactions, due to the localized surface plasmon resonance (LSPR) effect.<sup>15,16</sup> The LSPR effect enhances the visible light sensitivity of the materials and produces high-energy excitons that dissipate through the phonons, thereby resulting in high lattice temperature.<sup>17–19</sup> Such effects can lead to substantial improvement in the photocatalytic degradation efficiency.<sup>15,16</sup> The synergistic impact of Ag and AgCl, in which Ag nanoparticles work as an electron donor and AgCl promotes electron-hole pair separation and light absorption, boosts the photocatalytic degradation efficiency towards the target pollutant.<sup>20,21</sup> Zhou and coworkers discovered that Ag/AgCl/BiOCl degrades methyl orange (MO) by up to 97% in 60 minutes under visible light irradiation.<sup>22</sup> Zhao and coworkers also demonstrated that Ag/AgCl/BiOCl eliminates Rhodamine B (RhB) dye up to 97% in 50 minutes.<sup>23</sup>

Recent investigations have shown the exceptional photocatalytic degrading efficacy of BiOCl-based composites. Using a hydrothermal technique and *in situ* preparation, the Ag@ZnO/BiOCl composite was efficiently synthesized to study the photo-degradation of tetracycline hydrochloride. In the presence of simulated solar light, the modified sample has a degradation efficiency of 80.4%.<sup>24,25</sup>

Unfortunately, the complex structure and high durability of reactive dyes make photocatalytic degradation of reactive dyes extremely challenging. The principal goal of this work was to examine the photocatalytic degradation efficiency of a reactive dye (Reactive Orange 16) using a non-toxic photocatalyst that is prepared by using the co-precipitation technique. This study demonstrates the synthesis of different hybrid composites with different loadings of Ag–AgCl on BiOCl and the evaluation of their photocatalytic degradation efficiency for the elimination of Reactive Orange 16.

## 2. Materials and methods

### 2.1. Reagents and chemicals used

Reactive Orange 16 (RO16) was procured from Sisco Research Laboratory (SRL), India. Silver nitrate (AgNO<sub>3</sub>) and glacial acetic acid (CH<sub>3</sub>COOH, 99.5%) were sourced from Fisher Scientific.

Sodium chloride (NaCl) and bismuth nitrate pentahydrate [(Bi(NO<sub>3</sub>)<sub>3</sub>·5H<sub>2</sub>O)] were acquired from Loba Chemie Private Limited. Deionized water (DI) was produced utilizing the Milli-Q, Millipore ultrafiltration system. Absolute ethanol (99%) was purchased from Changshu Hongsheng Fine Chemicals Co. Ltd. Fluorinated tin oxide (FTO) glasses (resistance < 10 Ω) were procured from Vritra Technologies. Carbon black powder (CB) and polyvinylidene fluoride (PVDF) were bought from Nanoshell and Sigma Aldrich, respectively.

### 2.2. Preparation of BiOCl

The co-precipitation method was employed to synthesize bismuth oxychloride (BiOCl). Initially, 3 mmol (1.45 g) of Bi (NO<sub>3</sub>)<sub>3</sub>·5H<sub>2</sub>O was dissolved in 10 mL of glacial acetic acid. Solution A was produced by adding 30 mL of deionized water to the solution and stirring it for 1 hour after complete dissolution. To prepare solution B, 30 mL of DI water was combined with 3 mmol (0.175 g) of NaCl, stirring it for 1 hour. Solution B was subsequently added to solution A in a gradual, dropwise manner, resulting in the formation of white precipitates. After that, the suspension was subjected to stirring for 12 hours. The suspension was subsequently centrifuged. The desired BiOCl product was obtained by washing the precipitate thrice with DI water and ethanol and subsequently dried at 60 °C.<sup>26</sup>

### 2.3. Preparation of Ag–AgCl loaded BiOCl

Using a coprecipitation technique, Ag–AgCl/BiOCl was synthesized. For this, 3.25 g of Bi (NO<sub>3</sub>)<sub>3</sub>·5H<sub>2</sub>O was dissolved in 25 mL of glacial acetic acid. After complete dissolution, 75 mL of DI water was added to the above solution, and this solution was marked as A. Moreover, for solution B, 0.875 g of NaCl was dissolved in 75 mL of DI water. Both the solutions (solution A and B) were left to stir for 1 hour. For synthesizing AB1, 0.0325 g of AgNO<sub>3</sub> was added to solution A, and thereafter solution B was gradually poured into solution A to facilitate the precipitate formation. The final reaction mixture was allowed to stir for 16 hours (Scheme S1, ESI†). Afterward, the solid was separated by centrifugation and washed with DI water and ethanol, and dried at 60 °C. Similarly, 0.1625, 0.325, and 0.4875 g of silver nitrate were used to prepare AB5, AB10, and AB15 heterostructures, respectively.<sup>27</sup>

### 2.4. Preparation of thin films

Using the drop-cast method, the working electrodes for electrochemical impedance spectroscopy (EIS) were prepared. A smooth paste was achieved by mixing NMP (40–60 μL) and PVDF (1 mg). Additionally, 1 mg of CB was added and then blended for 15–20 min. Following this, 8 mg of the relevant material (BiOCl and AB10) was incorporated, resulting in a homogenous mixture. Afterward, the homogeneous paste was then drop-cast onto fresh FTO glass films and subsequently dried for 12 hours at 80 °C.



## 2.5. Characterization

A variety of characterization methods were employed to examine the crystallinity, composition, and surface morphology, along with other physicochemical properties of the synthesized photocatalyst. The crystallographic properties were evaluated using X-ray diffraction (XRD). The apparatus employed was an X'Pert pro24 Cu-K $\alpha$  (1.54 Å) operated at 45 kV, with a diffraction angle configured at 2 $\theta$  (5–90°). Energy dispersive spectroscopy (EDS) and field emission scanning electron microscopy (Carl-Zeiss Sigma 500, FESEM) were employed to analyse the structural morphology. Moreover, high-resolution transmission electron microscopy (JEOL JEM 2100 plus, HRTEM) was used to analyse the crystallinity and morphology. The oxidation states and electrical properties of the material were assessed using X-ray photoelectron spectroscopy (XPS). A UV-visible spectrophotometer (Shimadzu UV-2600) was employed to determine the diffused reflectance spectra (DRS). A mass spectrometer (Waters QTOF), equipped with XEVO G2 XS UHPLC and integrated APCI and ESI ionisation sources, was utilised for high-resolution mass spectrometry (HRMS) to detect the intermediates. Electrochemical impedance spectroscopy (EIS) tests were conducted in the dark at 0.55 V *vs.* RHE using a Biologic VSP300 potentiostat, within a frequency range of 1–10<sup>5</sup> Hz. The system comprised three electrodes: sample loaded on fluorine-doped tin (FTO) glasses, standard

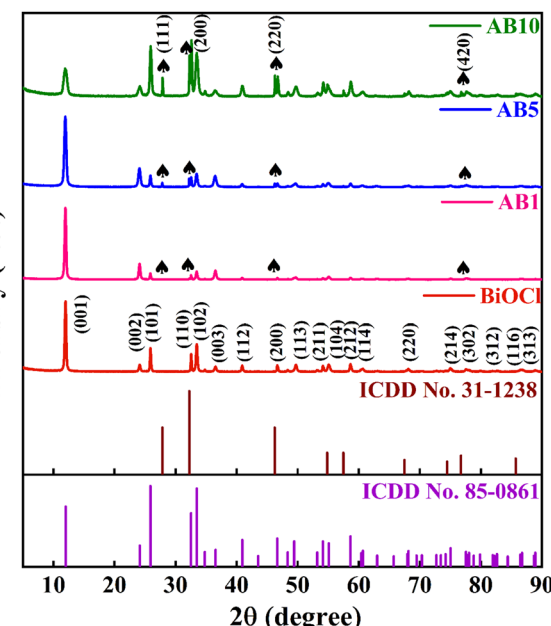


Fig. 2 XRD patterns of BiOCl, AB1, AB5, and AB10.

calomel electrode and platinum (Pt), which functioned as the working electrode, reference electrode and counter electrode, respectively, with 0.1 M sodium sulphate ( $\text{Na}_2\text{SO}_4$ ) solution.

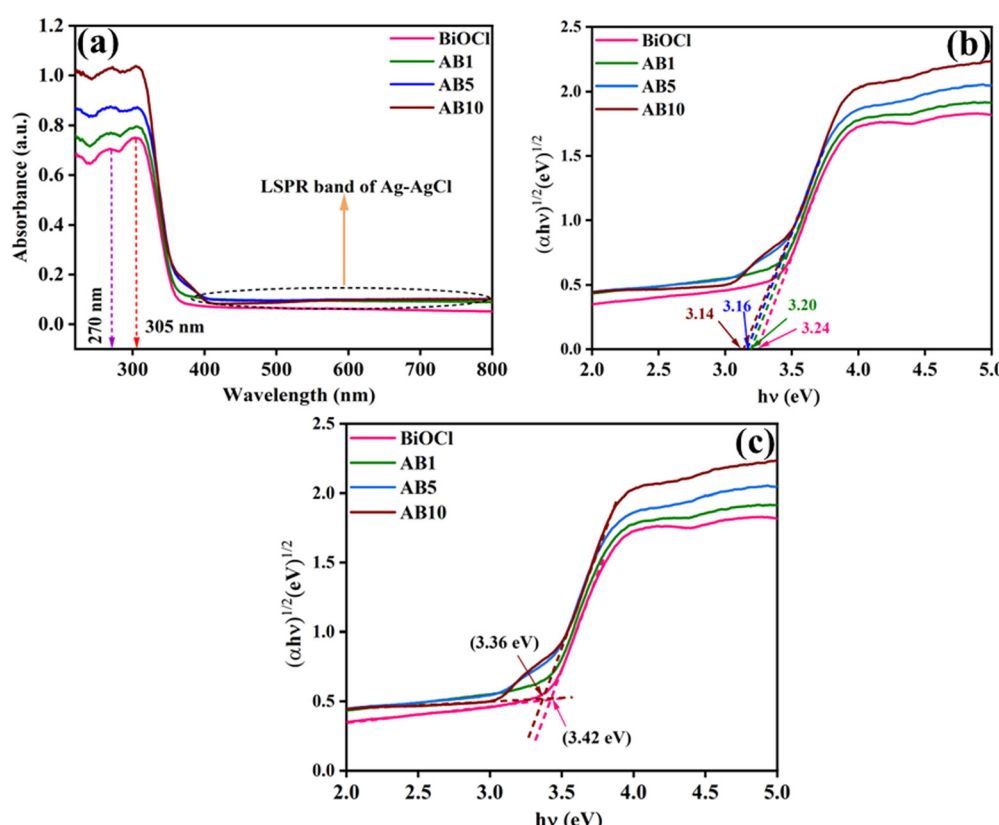


Fig. 1 (a) UV-visible DRS of BiOCl and hybrid-composites and Tauc plot showing (b) band gap and (c) band gap values at the adsorption edge.

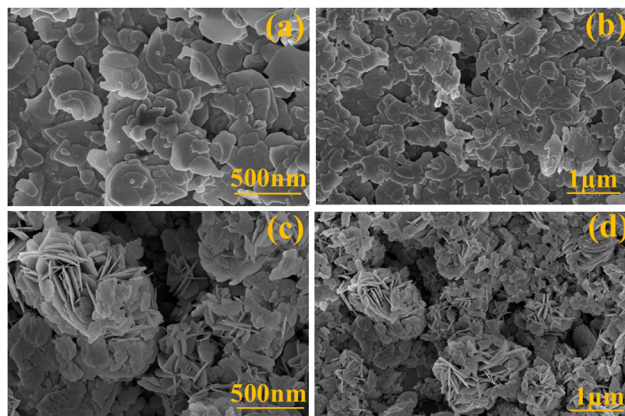


Fig. 3 FESEM images of BiOCl (a) and (b) and AB-10 (c) and (d).

## 2.6. Photodegradation studies

The degradation efficiencies of the synthesized catalysts towards photodegradation of RO16 were assessed in the presence of visible light. Initially, test tubes containing 10 mL of reactive dye solution were added with 7.5 mg of photocatalyst. Afterwards, the mixture was stirred for 30 minutes in the dark to ensure adsorption-desorption equilibrium. Subsequently, the reaction mixtures were irradiated with visible light using a Wipro Garnet B22-50 W LED (wavelength of greater than 360 nm and light intensity of 5000 lumens) for 90 minutes. Then the mixture was subsequently centrifuged to isolate the catalyst. The concentration of the reactive dyes was determined using a Shimadzu UV-2600 spectrometer for UV-visible spectroscopy by monitoring the absorbance at 490 nm.

The photodegradation efficiencies were computed by the following eqn (1)

$$\text{Photodegradation efficiency (\%)} = \frac{A_0 - A}{A_0} \times 100\% \quad (1)$$

where  $A_0$  = initial absorbance of the reaction mixture and  $A$  = final absorbance of the reaction mixture.

## 3. Results and discussion

### 3.1. DRS studies

UV-visible diffuse reflectance spectroscopy was used to study the optical properties of the prepared BiOCl and its composites. The absorption edge of BiOCl was measured within the region of 270–305 nm. Moreover, the electronic spectrum of AB10 exhibits a significant absorbance in the range of 400–800 nm, attributed to the LSPR effect of Ag–AgCl as illustrated in Fig. 1a, which can enhance the degradation efficiency considerably.<sup>28,29</sup> The bare BiOCl has a band position of 3.24 eV. The composites exhibit a gradual decrease in band gap from 3.24 eV to 3.14 eV, as illustrated in Fig. 1b. The band gap decreased to 3.14 eV when Ag–AgCl loading was increased to 10. The band gap values at the absorption edge were found to be in the range of 3.36 to 3.42 eV (Fig. 1c).

### 3.2. XRD studies

XRD analysis was executed to ascertain the phase purity and crystallinity of the prepared sample. Peaks were observed at 12.26°, 25.94°, 32.61°, 33.54°, 34.91°, 36.51°, 40.90°, 46.81°, 48.43°, 49.81°, 53.27°, 54.24°, 55.18°, 68.27°, 75.65°, and 77.72°, respectively. These  $2\theta$  values corresponded to the (001), (002), (101), (110), (102), (003), (112), (201), (113), (202), (211), (104), (212), (114), (214), and (310) planes, indicating tetragonal symmetry, which was well matched with the tetragonal BiOCl (ICDD no: 85-0861).<sup>16</sup> According to ICDD no. 31-1238, the planes (111), (200), (220), and (420) were seen at  $2\theta$  values of 27.9°, 32.2°, 46.3°, and 76.9°, respectively, which correlated to the formation of AgCl (Fig. 2).<sup>30,31</sup>

### 3.3. Morphology

FESEM was employed to examine the surface morphology of pure BiOCl and its composites with Ag–AgCl, the sample

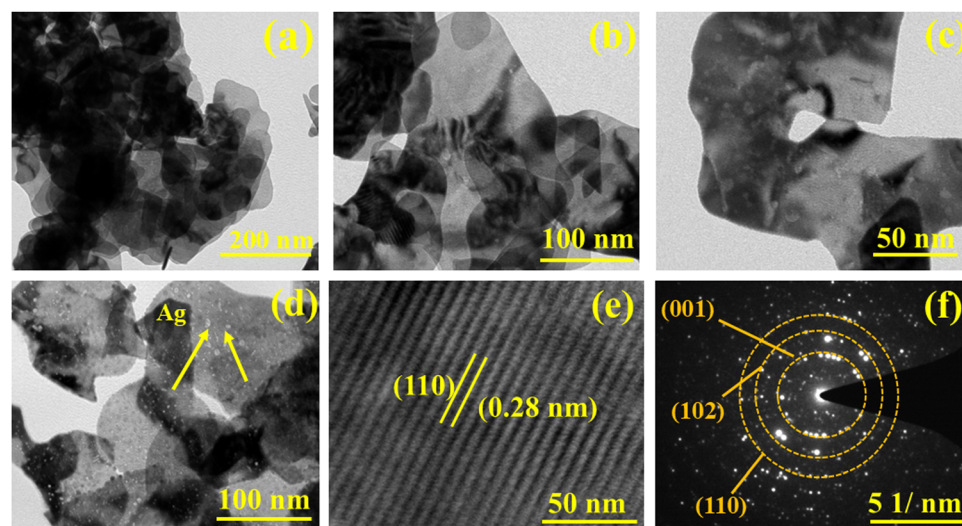


Fig. 4 (a)–(d) HRTEM images of AB-10, (e) lattice fringes and (f) SAED pattern.



labelled AB10, as illustrated in Fig. 3. Pure BiOCl exhibited an irregular, plate-like morphology, (Fig. 3a and b). Furthermore, (Fig. 3c and d), a flower-like shape is observed for Ag–AgCl–BiOCl. HRTEM was employed to assess the morphology and interior structures in greater detail (Fig. 4a–d). The HRTEM images clearly demonstrate the proper incorporation of pure BiOCl and Ag–AgCl particles. Additionally, it was found that the fringe width measured 0.28 nm (Fig. 4e),<sup>28,32</sup> which is characteristic of the crystallographic (110) plane of BiOCl, suggesting the retention of crystallinity in pure BiOCl within the

composite. The SAED pattern displays concentric rings with luminous spots, corresponding to the specific crystallographic planes (001), (102), and (110), which align with the tetragonal symmetry of BiOCl. This additionally confirms the development and crystallinity of the nanocomposite, as depicted in Fig. 4f. EDS mapping was utilized to determine the elemental composition of the synthesized catalyst. All components in Fig. S1 (ESI†) were uniformly distributed across the surface, demonstrating the absence of additional elements in the produced sample.

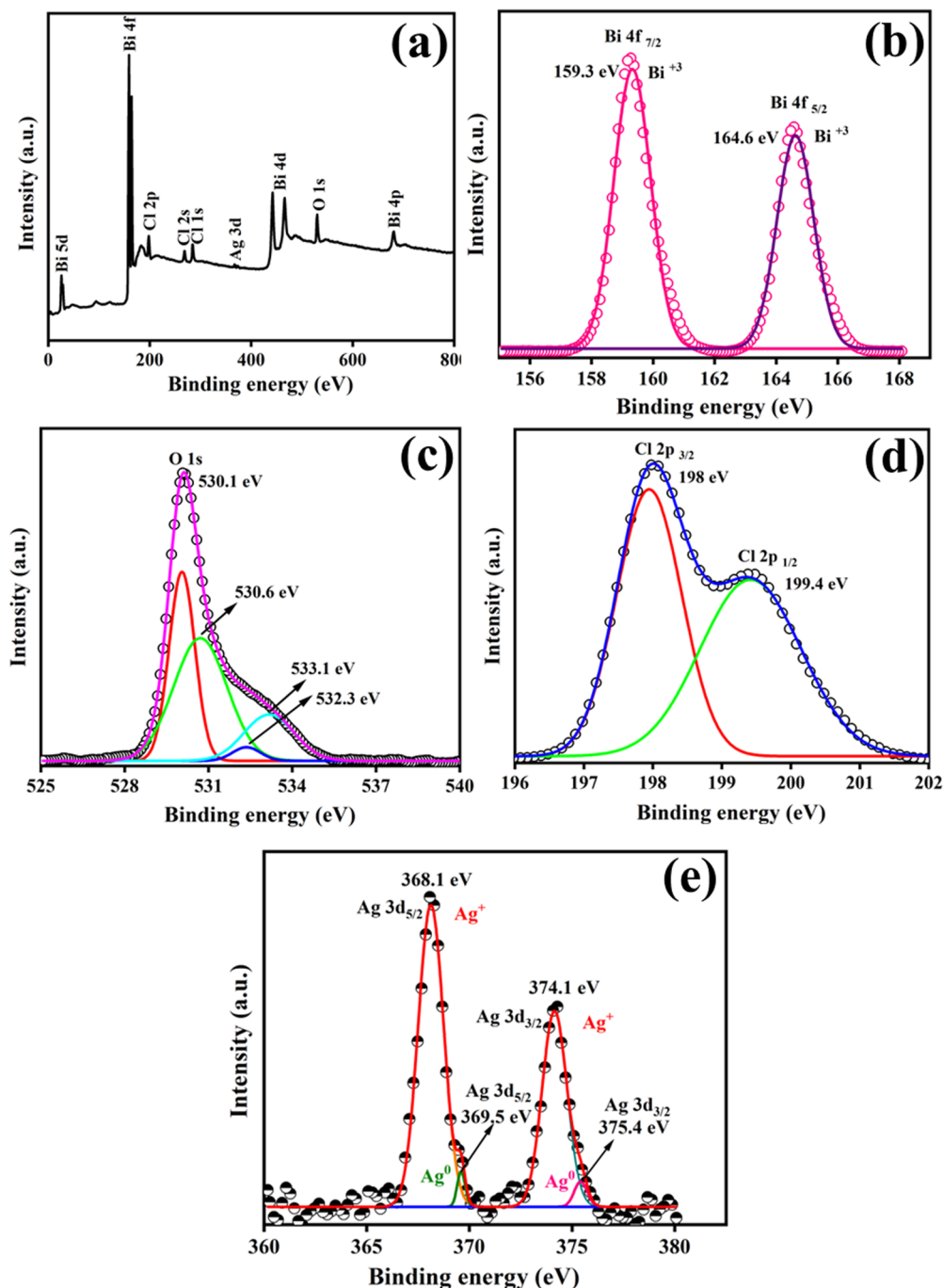


Fig. 5 XPS spectra of AB10 showing (a) survey spectrum, (b) Bi 4f, (c) O 1s, (d) Cl 2p and (e) Ag 3d patterns.



### 3.4. XPS studies

XPS studies were performed to study the atomic composition and oxidation states in AB10 (Fig. 5). All the constituent elements were in the sample based on the XPS survey spectrum, as shown in Fig. 5a. The existence of  $\text{Bi}^{3+}$  in the composite was confirmed by two distinct peaks, located at 159.3 eV and 164.6 eV, which are associated with  $\text{Bi} 4f_{7/2}$  and  $\text{Bi} 4f_{5/2}$ , respectively<sup>33,34</sup> (Fig. 5b). Additionally, the O 1s spectrum (Fig. 5c) has four binding energies at 530.1 eV and 530.6 eV, which confirms the presence of Bi–O and the O–Cl linkages, respectively.<sup>35</sup> Moreover, the peaks at 533.1 eV and 532.3 eV are characteristic of the physisorbed and chemisorbed water molecules, respectively (Fig. 5d). The Cl 2p signals at 198 eV and 199.4 eV are due to  $\text{Cl} 2p_{3/2}$  and  $\text{Cl} 2p_{1/2}$ , respectively; moreover, Ag 3d<sub>3/2</sub> and Ag 3d<sub>5/2</sub> signals (Fig. 5e) at 368.1 eV and 374.1 eV, respectively, confirm the presence of monovalent Ag. Furthermore, the analogous peaks at 375.4 eV and 369.5 eV indicate the presence of zerovalent silver in the composite.<sup>36</sup>

### 3.5. Photoluminescence spectra

The variation in electron–hole pair recombination in the synthesized catalysts was investigated using photoluminescence (PL) spectroscopy (Fig. 6). It was observed that the AB10 composite has much lower emission intensity. Such observation confirms that loading Ag–AgCl over the BiOCl surface reduces the charge carrier recombination rate.<sup>37</sup> Therefore, the AB10 heterostructure can act as a more efficient photocatalyst than the bare BiOCl.

### 3.6. EIS studies

EIS studies were performed in the dark on BiOCl and AB10 to investigate the parameters of charge separation. The Nyquist plot of AB10 has a smaller radius of AB10, indicating a more facile charge transfer in it compared to pristine BiOCl. Furthermore, these findings imply that the loading of Ag–AgCl facilitates the transfer of charge from BiOCl to its surface, thereby

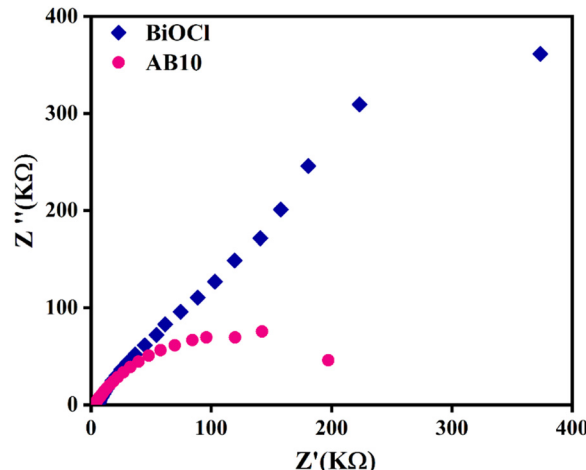


Fig. 7 EIS Nyquist plot of BiOCl and AB10.

lowering the resistance.<sup>38</sup> As a result, AB10 can work as an efficient catalyst (Fig. 7).

### 3.7. Photodegradation studies

To evaluate the photocatalytic degradation of pure BiOCl and its composites (AB1, AB5, AB10, and AB15) in the presence of visible light. Initially, the mixture was stirred in the dark for half an hour to achieve adsorption–desorption equilibrium. Moreover, visible light was exposed to the solution for 90 minutes. The degrading efficiency of pure BiOCl is quite low (Fig. 8a and b). This is explained by its limited capacity to reduce electron–hole pair recombination, which can restrict the number of active sites and, consequently, lower the degradation efficiency. However, from AB1 to AB10, the degradation efficiency steadily increases as the loading of Ag–AgCl on BiOCl increases due to less electron–hole pair recombination that allows charge separation, which increases the degradation efficiency to a higher degree (92%). Furthermore, due to the reduced active sites, a further increase in Ag–AgCl loading has no discernible effect on the photodegradation efficiency (Fig. S3, ESI† and Fig. 8b). All the photocatalytic reactions obey the pseudo-zero order kinetic model (eqn (2)),<sup>39</sup> (Fig. 8c and Table S1, ESI†).

$$C_t = C_0 - kt \quad (2)$$

where  $C_t$  = the concentration at time 't',  $C_0$  = the concentration at time  $t = 0$ , and  $k$  = rate constant for the pseudo zero order reaction.

Furthermore, it was observed that AB10 has the greatest rate constant value of  $0.438(2) \text{ mol L}^{-1} \text{ min}^{-1}$ , as demonstrated in Fig. 8d. Additionally, the values of half-life were found to vary linearly with initial concentration, hence confirming the validity of the pseudo zero order kinetics further (Fig. S4, ESI†).

To optimize catalyst utilization, the amount of catalyst used for the degradation of Reactive Orange 16 was adjusted, and a difference in degradation efficiency was noticed. As the amount of catalyst increased, the photocatalytic degradation efficiency dropped, as illustrated in Fig. 9. There were more active sites up

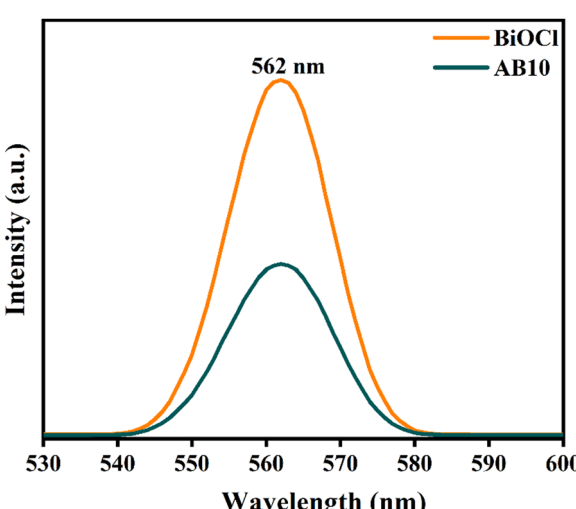


Fig. 6 PL spectra of BiOCl and AB10.



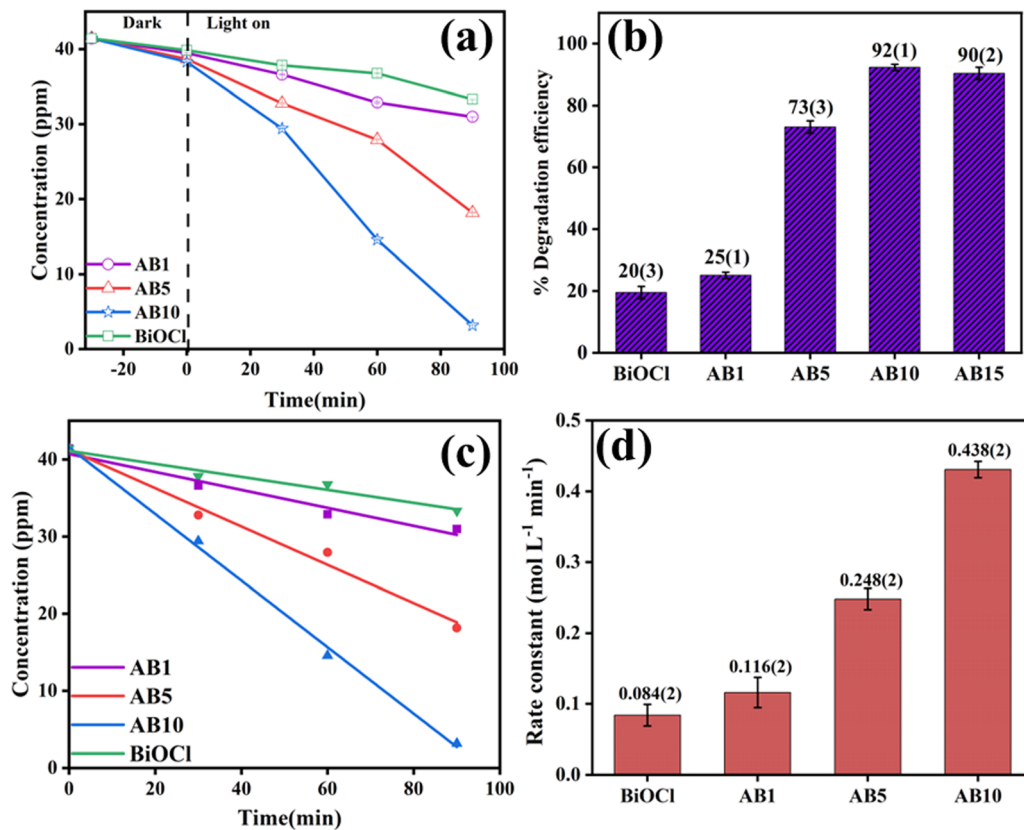


Fig. 8 (a) Variation in concentration of RO16 with time of all the samples. (b) Comparison of degradation efficiency of all the photocatalysts. (c) Pseudo-zero-order kinetic model fitting and (d) comparison of the rate constant values of BiOCl, AB1, AB5, and AB10.

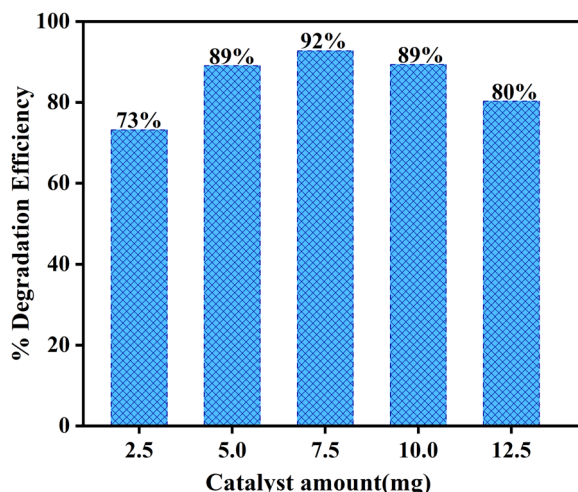


Fig. 9 Effect of catalyst loading towards Reactive Orange 16.

to 7.5 mg, resulting in the highest photocatalytic degradation efficiency possible. As the concentration increased, particles accumulated, thereby clogging the active sites and reducing the degradation efficiency. As a result, a dosage of 7.5 mg of the catalyst and pollutant concentrations of 40 ppm were used for subsequent studies.<sup>40</sup>

### 3.8. Mechanistic details

**3.8.1. Proposed mechanism.** Based on the above findings, the hypothesized photocatalytic degradation mechanism is

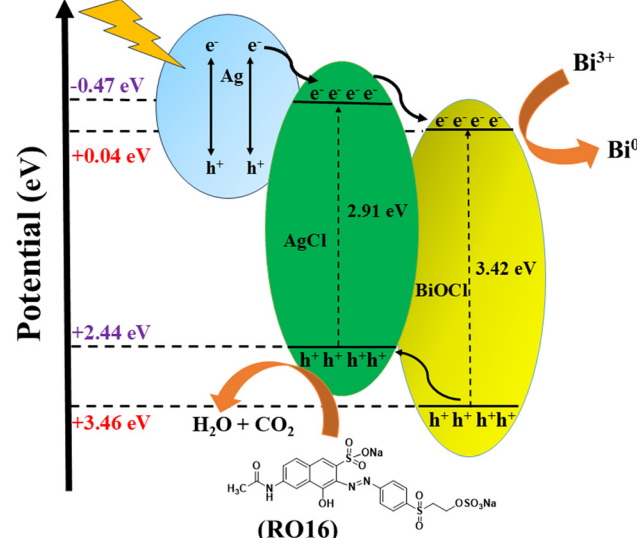


Fig. 10 Proposed mechanistic representation for the photocatalytic degradation of RO16.

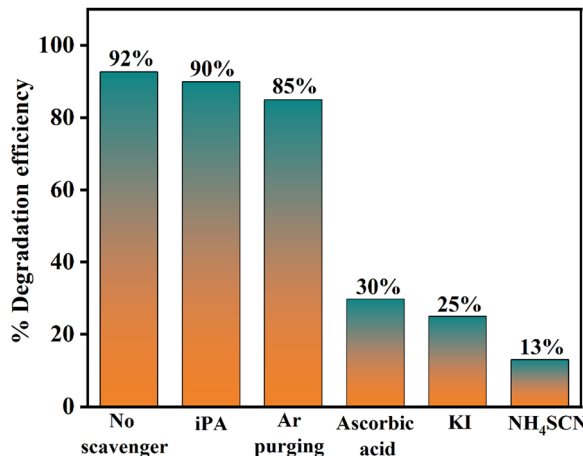


Fig. 11 Variation in degradation efficiency after Ar purging and addition of ascorbic acid, KI, and NH<sub>4</sub>SCN.

based on electron–hole pair recombination. The band gap was determined with the following equation:

$$E_{VB} = \chi - E_e + 0.5E_g \quad (3)$$

$$E_{CB} = E_{VB} - E_g \quad (4)$$

where  $E_{VB}$  represents the valence band potential,  $E_{CB}$  depicts the conduction band potential,  $\chi$  is the electronegativity of the material,  $E_g$  = band gap energy, and  $E_e$  = energy of a free electron.

The  $E_{VB}$  values at the absorption edge for BiOCl and AgCl are +3.46 eV and +2.44 eV, respectively, whereas the  $E_{CB}$  value for BiOCl is +0.04 eV and −0.47 eV for AgCl. Therefore, BiOCl

possesses a more positive electrode potential as compared to AgCl.<sup>41–45</sup> The proposed mechanism involves electrons being excited from the VB to the CB in order to produce an electron–hole pair (Fig. 1c and 10), followed by the electron transfer from the CB of AgCl to the CB of BiOCl and the hole transfer from the VB of BiOCl to the VB of AgCl. The CB edge potential of BiOCl (+0.04 eV) is less negative than the superoxide radical (−0.046 eV), whereas the VB edge potential of AgCl (+2.44) is less positive than  $\cdot\text{OH}/\text{H}_2\text{O}$  (+2.68 eV). As a result, the oxidation of  $\text{H}_2\text{O}$  to hydroxyl radicals and the reduction of dissolved oxygen to superoxide anions are not feasible. The dye (Reactive Orange 16) can get oxidized by holes only, while metal cations can act as an electron scavenger.

**3.8.2. Scavenger studies.** To support the proposed mechanism, several controlled studies were conducted. In the presence of hole scavengers like NH<sub>4</sub>SCN, KI, and ascorbic acid, the degradation efficiency drops to 13%, 25%, and 30%, respectively, whereas upon addition of IPA (isopropyl alcohol) and Ar purging, there was significantly less or no change in the degradation efficiency as shown in Fig. 11. As a result, holes play a vital part, whereas electrons, superoxides, and hydroxide radicals do not play any major role in the mechanism.

**3.8.3. Characterization of the recovered catalyst.** In order to confirm the reduction of metal ions, XRD, DRS, and XPS of the recovered catalyst were performed (Fig. 12). The XRD pattern of the recovered catalyst shows three extra peaks centered at 38.1°, 44.3°, and 64.6°, which indicate the presence of metallic bismuth (Fig. 12a).<sup>46,47</sup> Furthermore, in DRS an intense LSPR band of metallic bismuth was found, as observed in Fig. 12b. Moreover, the band gap of the recovered catalyst becomes slightly smaller compared to the original one (Fig. S7,

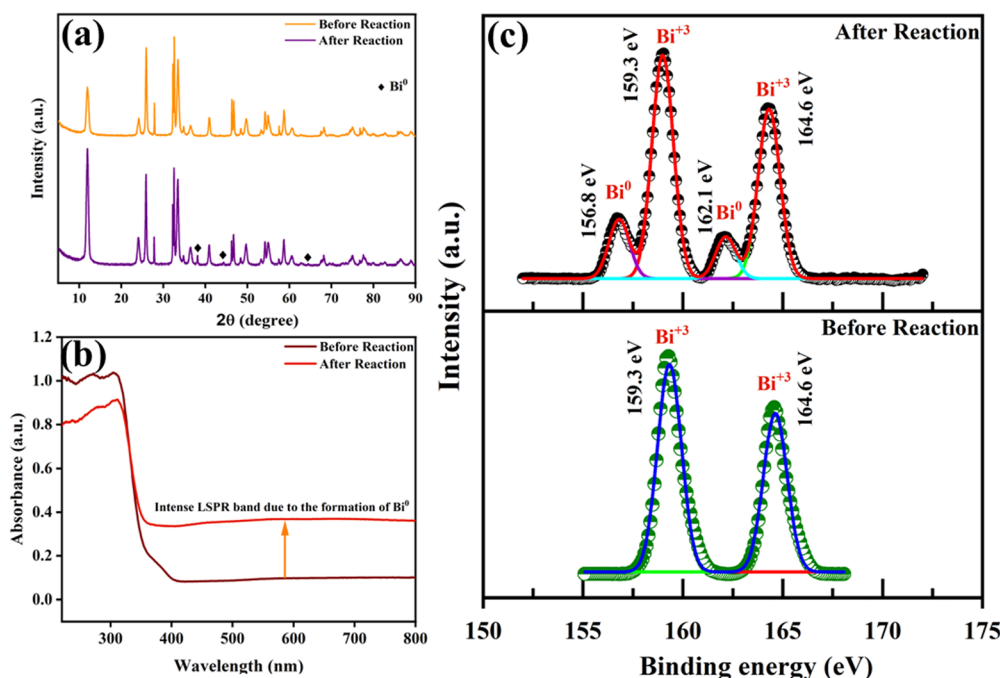
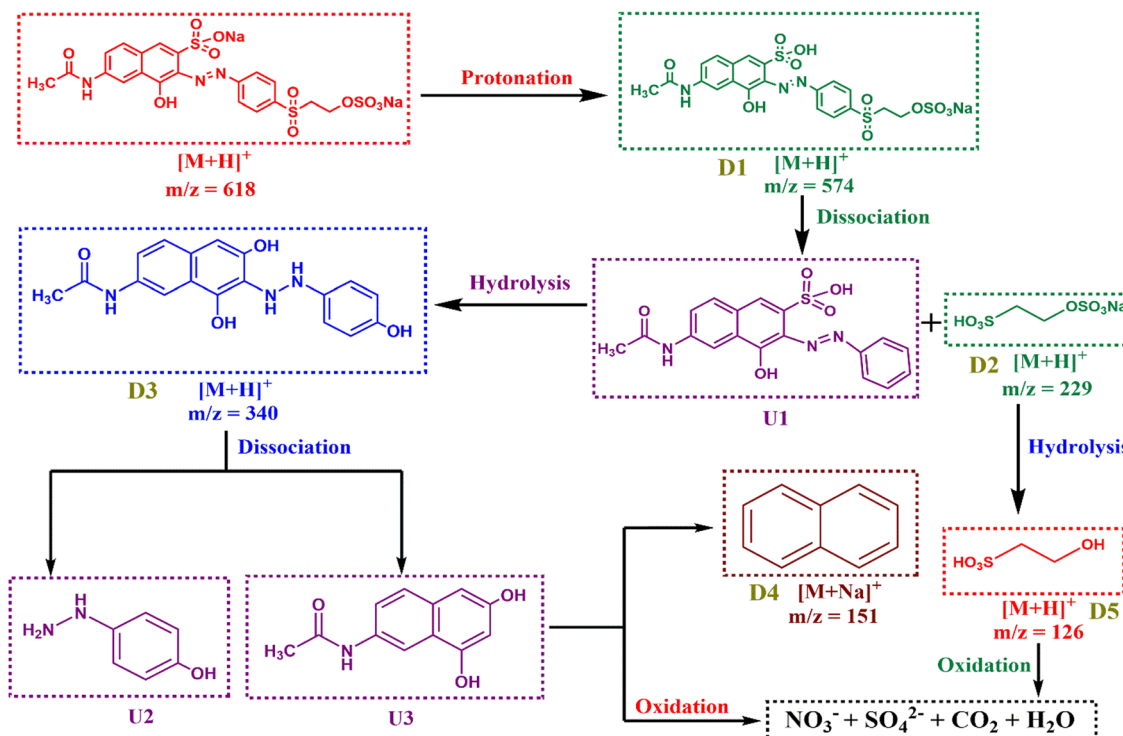


Fig. 12 (a) XRD, (b) DRS and (c) XPS patterns of AB10 before and after the reaction.





Scheme 1 Proposed mechanism for the photocatalytic degradation of RO16 utilizing AB10 (D1 to D6 signifies detected fragments, and U1 to U3 depicts unidentified fragments).

ESI†). The XPS studies also confirmed the formation of zerovalent bismuth as evident from the occurrence of new signals at 156.8 eV and 162.1 eV as illustrated in Fig. 12c.<sup>48,49</sup>

**3.8.4. HRMS studies.** In order to identify the intermediates, HPLC-MS experiments were conducted to gather a deeper insight into the mechanism (Scheme 1 and Fig. S5, S6, ESI†). The characteristic peaks of the anionic and protonated form of Reactive Orange 16 dye were observed at  $m/z$  618 and 574 (D1), respectively. Furthermore, the peaks observed at  $m/z$  229 (D2), 340 (D3), 151 (D4), and 126 (D5) correspond to various smaller fragments formed during the photocatalytic reactions. It has

been observed that the intensity corresponding to the smaller fragment increases with time. Such observations confirm the photodegradation of RO16.

### 3.9. Reusability and stability of the catalyst

To investigate potential future uses, the stability and reusability of the photocatalyst are crucial. At the end of the reaction, the catalyst was recovered from the reaction mixture and utilized further. It was found that the photodegradation efficiency of AB10 declined to only 4% (Fig. 13) from the first to fourth cycle. Such observation suggests that the AB10 catalyst has excellent reusability towards the elimination of RO16. The minor decrease in the removal efficiency can be ascribed to catalyst loss during recovery.

In order to determine the stability of the synthesized catalyst (AB10), FESEM studies were performed. It has been observed that there are no significant changes in the morphology of the as-prepared catalyst before and after the reaction (Fig. 14).

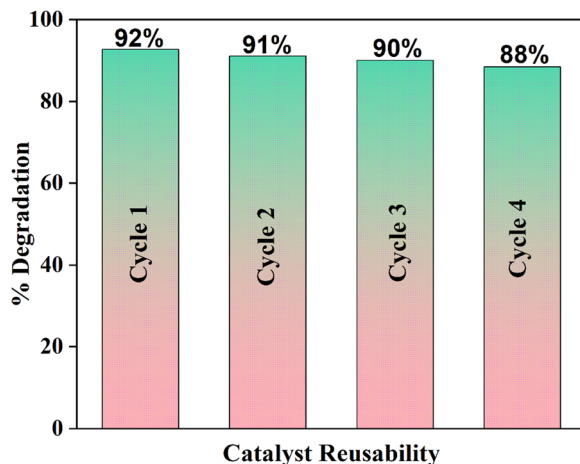


Fig. 13 Reusability of AB10 up to four cycles.

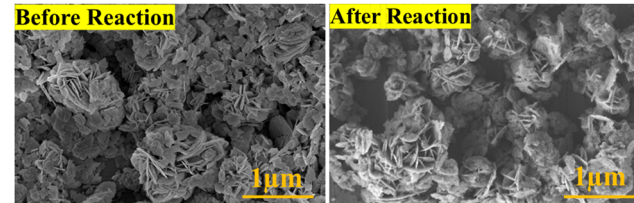


Fig. 14 FESEM of AB10 before and after reaction.

Table 1 Comparison of the photocatalytic degradation efficiency of several reported catalysts towards Reactive Orange 16

S. no.	Catalyst	Reactive dyes	Catalyst dosage (mg L <sup>-1</sup> )	Intensity of light (W m <sup>-2</sup> )	Degradation efficiency (%)	Light source	Reaction time (min)	Ref.
1	gC <sub>3</sub> N <sub>4</sub> -MU	RO16	1000	55	95	Visible light	60	50
2	MgO/gC <sub>3</sub> N <sub>4</sub>	RO16	400	39.6	82	Visible light	30	51
3	Ag/AgVO <sub>4</sub> /AgVO <sub>3</sub>	RO16	1000	300	97	Visible light	200	52
4	CeO <sub>2</sub> /ZnO	RO16	2000	300	90	Visible light	180	53
5	S <sub>x</sub> N <sub>x</sub> co-doped TiO <sub>2</sub> /graphene	RO16	333.33	500	96	Visible light	120	54
6	Ag-AgCl/BiOCl	RO16	750	50	92	Visible light	90	This work

These observations confirm the high stability of the photocatalysts.

### 3.10. Comparison of the degradation efficiencies

The synthesized photocatalyst (AB10) has been compared with the existing literature (Table 1). It has to be noted that apart from a few catalysts, our catalyst shows comparable or better photocatalytic efficiency. However, most of these either need a larger dosage of catalyst,<sup>47,49</sup> higher light intensity,<sup>47,49–51</sup> or longer reaction time.<sup>49,51</sup> Such observation shows that compared to the reported literature the AB10 composite shows a superior photocatalytic activity.

## 4. Conclusions

In conclusion, this study demonstrates that Ag–AgCl–BiOCl was synthesized utilizing a straightforward co-precipitation technique for the removal of RO16 in the presence of visible light. The controlled studies indicate that the holes were involved in the entire mechanism. The HRMS tests show smaller fragments for photocatalytic degradation of pollutants, which provides further information on the mechanism. During the procedure, Bi (+3) was reduced to Bi(0), causing the LSPR effect as observed in the DRS of the recovered photocatalyst. Furthermore, the photocatalyst produced is very recyclable and stable. Owing to its low cost, low toxicity, and high catalytic activity, the synthesized catalyst could be useful for eliminating reactive dyes from wastewater.

## AI tools

The grammatical mistakes have been checked and amended using the Grammarly tool.

## Author contributions

Kamya Jasuja: writing the original draft, visualization, validation, investigation, formal analysis, data curation, and conceptualization. Raj Kumar Das: writing – review & editing, visualization, validation, supervision, resources, funding acquisition, and conceptualization.

## Data availability

The supporting data have been uploaded as part of the ESI.†

## Conflicts of interest

The authors declare that they have no known competing financial interests or personal relationships that could have appeared to influence the work reported in this paper.

## Acknowledgements

This work is supported by the TIET VT CEEMS Research grant. The authors express gratitude to Sai Labs, TIET, for conducting the XRD measurements. The authors express profound gratitude to the Department of Physics and Material Science for providing SEM-EDS measurements and sprint testing solutions for XPS and HRTEM studies. The authors express gratitude to DST-FIST (Infrastructure Grant number: SR/FST/CS-II/2018/69) for the HRMS facility. The authors express their gratitude to Prof. Bonamali Pal and Prof. Satnam Singh for providing access to their laboratory facilities. Also, the authors are thankful to Dr Banibrata Maity and Ms Malika Phull for the PL analysis. The authors express their gratitude to Prof. B. N. Chudasama and Ms Neha Saini for their contributions to the DRS characterization. The authors express their gratitude to Mr Samarjit Mandal for supplying the ICDD data. The authors express profound gratitude to Prof. O. P. Pandey and Mr Abhishek Chandel for their contributions to EIS characterization.

## References

- 1 H. A. Kiwaan, T. M. Atwee, E. A. Azab and A. A. El-Binary, Photocatalytic degradation of organic dyes in the presence of nanostructured titanium dioxide, *J. Mol. Struct.*, 2020, **1200**, 127115.
- 2 D. K. Bhatt and U. D. Patel, Photocatalytic degradation of Reactive Black 5 using Ag<sub>3</sub>PO<sub>4</sub> under visible light, *J. Phys. Chem. Solids*, 2021, **149**, 109768.
- 3 Y. Wu, M. Ruan, C. Wang, T. Zhong and Z. Liu, Construction of 2D/2D BiOIO<sub>3</sub>/Bi<sub>2</sub>O<sub>2</sub>CO<sub>3</sub> composite structures with face-to-face contacts can facilitate carrier transfer via a built-in electric field and a polar field for pyro-photo-electric catalysis, *J. Mater. Chem. C*, 2024, **12**, 13010–13020.
- 4 Y. Wu, M. Ruan, Z. Guo, C. Wang and Z. Liu, Optimization of the IO<sub>3</sub> polar group of BiOIO<sub>3</sub> by bulk phase doping amplifies pyroelectric polarization to enhance carrier separation and improve the pyro-photo-electric catalytic performance, *Appl. Catal., B*, 2023, **339**, 123169.



5 Y. G. Alghamdi, B. Krishnakumar, M. A. Malik and S. Alhayyani, Design and Preparation of Biomass-Derived Activated Carbon Loaded  $\text{TiO}_2$  Photocatalyst for Photocatalytic Degradation of Reactive Red 120 and Ofloxacin, *Polymers*, 2022, **14**, 880.

6 M. F. Lanjwani, M. Tuzen, M. Y. Khuhawar and T. A. Saleh, Trends in photocatalytic degradation of organic dye pollutants using nanoparticles: A review, *Inorg. Chem. Commun.*, 2024, **159**, 11613.

7 R. Frei, K. Heye and C. Roduit, Environmental influences on childhood allergies and asthma—The Farm effect, *Pediatr. Allergy Immunol.*, 2022, **33**, 13807.

8 Ö. F. Ertuğrul and M. F. Akil, Detecting hemorrhage types and bounding box of hemorrhage by deep learning, *Biomed. Signal Process. Control*, 2022, **71**, 103085.

9 J. S. D. Santos, J. P. G. Cirino, P. D. O. Carvalho and M. M. Ortega, The Pharmacological Action of Kaempferol in Central Nervous System Diseases: A Review, *Front. Pharmacol.*, 2021, **11**, 2020.

10 B. A. Labib and D. I. Chigbu, Therapeutic Targets in Allergic Conjunctivitis, *Pharmaceuticals*, 2022, **15**, 547.

11 E. Erusappan, S. Thiripuranthagan, R. Radhakrishnan, M. Durai, S. Kumaravel, T. Vembuli and N. J. Kaleekkal, Fabrication of mesoporous  $\text{TiO}_2$ /PVDF photocatalytic membranes for efficient photocatalytic degradation of synthetic dyes, *J. Environ. Chem. Eng.*, 2021, **9**, 105776.

12 T. Song, X. Yu, N. Tian and H. W. Huang, Preparation, structure and application of g-C<sub>3</sub>N<sub>4</sub>/BiOX composite photocatalyst, *Int. J. Hydrogen Energy*, 2021, **46**, 1857–1878.

13 T. Alapi, B. Veres, M. Náfrádi, L. Farkas, Z. Pap and A. Covic, Application of BiOX Photocatalyst to Activate Peroxydisulfate Ion-Investigation of a Combined Process for the Removal of Organic Pollutants from Water, *Catalysts*, 2023, **13**, 513.

14 D. O. Adenuga, S. M. Tichapondwa and E. M. N. Chirwa, Facile synthesis of a Ag/AgCl/BiOCl composite photocatalyst for visible-light-driven pollutant removal, *J. Photochem. Photobiol. A*, 2020, **401**, 112747.

15 W. Zhu, J. Song, X. Wang, Y. Lu, G. Hu and J. Yang, The fast degradation for tetracycline over the Ag/AgBr/BiOBr photocatalyst under visible light, *J. Mater. Sci.: Mater. Electron.*, 2021, **32**, 26465.

16 Y. Wu, T. Zhong, M. Ruan, C. Wang and Z. Liu, Optimization of carrier transfer kinetics of  $\text{BiOIO}_3$  using TFA/TFA-reversible redox pairs of TFA molecules as co-catalysts for efficient photoelectrochemical water splitting system, *Int. J. Hydrogen Energy*, 2024, **88**, 571–578.

17 R. Li, X. Wang and M. Chen, Non-Noble Metal and Non-metallic Plasmonic Nanomaterials with Located Surface Plasmon Resonance Effects: Photocatalytic Performance and Applications, *Catalysts*, 2023, **13**, 940.

18 Z. Zhang, C. Zhang, H. Zheng and H. Xu, Plasmon-Driven Catalysis on Molecules and Nanomaterials, *Acc. Chem. Res.*, 2019, **52**, 2506–2515.

19 Z. Zheng, W. Xie, B. Huang and Y. Dai, Plasmon-Enhanced Solar Water Splitting on Metal-Semiconductor Photocatalysts, *Chem. – Eur. J.*, 2018, **24**, 18322–18333, DOI: [10.1002/chem.201803705](https://doi.org/10.1002/chem.201803705).

20 Z. Xu and S. Y. Lin, Construction of AgCl/Ag/BiOCl with a concave-rhombicuboctahedron core-shell hierarchitecture and enhanced photocatalytic activity, *RSC Adv.*, 2016, **6**, 84738–84747.

21 Y. Huang, S. Kang, Y. Yang, H. Qin, Z. Ni, S. Yang and X. Li, Facile synthesis of Bi/Bi<sub>2</sub>WO<sub>6</sub> nanocomposite with enhanced photocatalytic activity under visible light, *Appl. Catal., B*, 2016, **196**, 89–99.

22 S. Zou, X. Mao, L. Wu, Y. Li, J. Li, J. Yang and X. Fan, Deposition of Ag@AgCl onto Flower-Like BiOCl for Promoting the Degradation of Methyl Orange: The Narrow Bandgap and Surface Plasmon Resonance Effect, *Korean J. Chem. Eng.*, 2024, **41**, 2705–2715.

23 S. Zhao, Y. Zhang, Y. Zhou, K. Qiu, C. Zhang, J. Fang and X. Sheng, Reactable polyelectrolyte-assisted preparation of flower-like Ag/AgCl/BiOCl composite with enhanced photocatalytic activity, *J. Photochem. Photobiol. A*, 2018, **350**, 94–102.

24 Z. Zhang, A. Zada, N. Cui, N. Liu, M. Liu, Y. Yang, D. Jiang, J. Jiang and S. Liu, Synthesis of ag loaded ZnO/BiOCl with high photocatalytic performance for the removal of antibiotic pollutants, *Crystals*, 2021, **11**, 981.

25 X. Zhang, Y. Huo, M. Shakeel, B. Li, L. Wang, J. Liu and S. Zuo, Fabrication of BiOCl/ZnO/CN Nanocomposite for Visible-Light Photocatalytic Degradation of Dyes, *Chemistry-Select*, 2020, **5**, 1640–1647.

26 J. Wang and Z. Zhang, Co-precipitation synthesis and photocatalytic properties of BiOCl microflowers, *Optik*, 2020, **204**, 164149.

27 M. Anwar, K. S. Alghamdi, S. Zulfiqar, M. F. Warsi, M. Waqas and M. Hasan, Ag-decorated BiOCl anchored onto the g-C<sub>3</sub>N<sub>4</sub> sheets for boosted photocatalytic and antimicrobial activities, *Opt. Mater.*, 2023, **135**, 113336.

28 L. Liang, Y. Lv, Z. Yu, R. Wu, Q. Shi, H. Chen and J. Wang, Surface plasmon resonance effect of Ag@BiOCl and its enhanced visible light-photodegradation of acid red B, *J. Mater. Sci.: Mater. Electron.*, 2021, **32**, 18646–18656.

29 D. Wei, F. Tian, Z. Lu, H. Yang and R. Chen, Facile synthesis of Ag/AgCl/BiOCl ternary nanocomposites for photocatalytic inactivation of S. aureus under visible light, *RSC Adv.*, 2016, **6**, 52264–52270.

30 W. Zhang, X. Dong, Y. Liang, Y. Sun and F. Dong, Ag/AgCl nanoparticles assembled on BiOCl/Bi<sub>12</sub>O<sub>17</sub>Cl<sub>2</sub> nanosheets: Enhanced plasmonic visible light photocatalysis and *in situ* DRIFTS investigation, *Appl. Surf. Sci.*, 2018, **455**, 236–243.

31 S. Kota, P. Dumpala, R. K. Anantha, M. K. Verma and S. Kandepu, Evaluation of therapeutic potential of the silver/silver chloride nanoparticles synthesized with the aqueous leaf extract of Rumex acetosa, *Sci. Rep.*, 2017, **7**, 11566.

32 L. Wang, D. Lv, Z. Yue, H. Zhu, L. Wang, D. Wang, X. Xu, W. Hao, S. X. Dou and Y. Du, Promoting photoreduction properties via synergistic utilization between plasmonic



effect and highly active facet of BiOCl, *Nano Energy*, 2019, **57**, 398–404.

33 P. Rohilla, B. Pal and R. K. Das, Bi-doped  $g\text{-C}_3\text{N}_4/\text{Bi}_2\text{WO}_6$  ternary composites for superior photocatalytic degradation of reactive orange 16 under visible light irradiation, *J. Ind. Eng. Chem.*, 2024, **57**, 398.

34 P. Rohilla, B. Pal and R. K. Das, Improved photocatalytic degradation of rhodamine B by  $g\text{-C}_3\text{N}_4$  loaded  $\text{BiVO}_4$  nanocomposites, *Helijon*, 2023, **9**, e21900.

35 A. Phuruangrat, T. Thongtem and S. Thongtem, Microwave-assisted deposition synthesis, characterization and photocatalytic activities of UV-light-driven Ag/BiOCl nanocomposites, *Inorg. Nano-Met. Chem.*, 2021, **51**, 1813–1821.

36 J. Wang, C. An, M. Zhang, C. Qin, X. Ming and Q. Zhang, Photochemical conversion of  $\text{AgCl}$  nanocubes to hybrid  $\text{AgCl}\text{-Ag}$  nanoparticles with high activity and long-term stability towards photocatalytic degradation of organic dyes, *Can. J. Chem.*, 2012, **90**, 858–864.

37 X. Xu, Q. Yan, X. Gu and Y. Luo, The preparation and photocatalytic performance of  $\text{BiOCl@Ag}$ , a visible-light responsive catalyst, *J. Mater. Sci.: Mater. Electron.*, 2019, **30**, 8892–8902.

38 A. Zulkiflee, M. M. Khan, A. Khan, M. Y. Khan, H. D. M. Dafalla and M. H. Harunsani, Sn-doped BiOCl for photoelectrochemical activities and photocatalytic dye degradation under visible light, *Helijon*, 2023, **9**, e21270.

39 M. Anjum, R. Kumar, S. M. Abdelbasir and M. A. Barakat, Carbon nitride/titania nanotubes composite for photocatalytic degradation of organics in water and sludge: Pre-treatment of sludge, anaerobic digestion and biogas production, *J. Environ. Manage.*, 2018, **223**, 495–502.

40 M. Bansal, K. Jasuja and R. K. Das, Photocatalytic degradation of reactive dyes over Ni-Al layered double hydroxide, *Catal. Commun.*, 2024, **187**, 106879.

41 L. Cai, Enhanced visible light photocatalytic activity of BiOCl by compositing with  $g\text{-C}_3\text{N}_4$ , *Mater. Res. Innovations*, 2015, **19**, 392–396.

42 N. Chang, Y. R. Chen, F. Xie, Y. P. Liu and H. T. Wang, Facile construction of Z-scheme  $\text{AgCl}/\text{Ag}$ -doped-ZIF-8 heterojunction with narrow band gaps for efficient visible-light photocatalysis, *Colloids Surf. A*, 2021, **616**, 126351.

43 A. Kundu, S. Sharma and S. Basu, Modulated BiOCl nanoplates with porous  $g\text{-C}_3\text{N}_4$  nanosheets for photocatalytic degradation of color/colorless pollutants in natural sunlight, *J. Phys. Chem. Solids*, 2021, **154**, 110064.

44 Y. Chen, G. Zhu, Y. Liu, J. Gao, C. Wang, R. Zhu and P. Liu, Preparation of hollow  $\text{Ag}/\text{AgCl}/\text{BiOCl}$  microspheres with enhanced photocatalytic activity for methyl orange under LED light irradiation, *J. Mater. Sci.: Mater. Electron.*, 2017, **28**, 2859–2866.

45 Y. Li, Z. Liu, Z. Guo, M. Ruan, X. Li and Y. Liu, Efficient  $\text{WO}_3$  Photoanode Modified by Pt Layer and Plasmonic Ag for Enhanced Charge Separation and Transfer to Promote Photoelectrochemical Performances, *ACS Sustainable Chem. Eng.*, 2019, **7**, 12582–12590.

46 Z. Zhao, W. Zhang, Y. Sun, J. Yu, Y. Zhang, H. Wang, F. Dong and Z. Wu, Bi Cocatalyst/ $\text{Bi}_2\text{MoO}_6$  Microspheres Nanohybrid with SPR-Promoted Visible-Light Photocatalysis, *J. Phys. Chem. C*, 2016, **120**, 11889–11898.

47 S. Tao, S. Sun, T. Zhao, J. Cui, M. Yang, X. Yu, Q. Yang, X. Zhang and S. Liang, One-pot construction of Ta-doped  $\text{BiOCl}/\text{Bi}$  heterostructures toward simultaneously promoting visible light harvesting and charge separation for highly enhanced photocatalytic activity, *Appl. Surf. Sci.*, 2021, **543**, 148798.

48 P. Kumari, R. K. Das and B. Pal, Enhanced photocatalytic degradation of eco-toxic pharmaceutical waste diclofenac sodium by anion loaded Cu-Al LDH- $\text{Bi}_2\text{O}_3$  composites, *J. Taiwan Inst. Chem. Eng.*, 2021, **129**, 227–236.

49 R. A. Rather, S. Singh and B. Pal, A  $\text{Cu}^{+1}/\text{Cu}^0\text{-TiO}_2$  mesoporous nanocomposite exhibits improved  $\text{H}_2$  production from  $\text{H}_2\text{O}$  under direct solar irradiation, *J. Catal.*, 2017, **346**, 1–9.

50 M. Solehudin, U. Sirimahachai, G. A. M. Ali, K. F. Chong and S. Wongnawa, One-pot synthesis of isotype heterojunction  $g\text{-C}_3\text{N}_4\text{-MU}$  photocatalyst for effective tetracycline hydrochloride antibiotic and reactive orange 16 dye removal, *Adv. Powder Technol.*, 2020, **31**, 1891–1902.

51 E. Fathi, F. Derakhshanfar, P. Gharbani and Z. G. Tabatabaei, Facile Synthesis of  $\text{MgO}/\text{C}_3\text{N}_4$  Nanocomposite for Removal of Reactive Orange 16 Under Visible Light, *J. Inorg. Organomet. Polym. Mater.*, 2020, **30**, 2234–2240.

52 B. H. Fard, R. R. Khojasteh and P. Gharbani, Preparation and Characterization of Visible-Light Sensitive Nano  $\text{Ag}/\text{Ag}_3\text{VO}_4/\text{AgVO}_3$  Modified by Graphene Oxide for Photodegradation of Reactive Orange 16 Dye, *J. Inorg. Organomet. Polym. Mater.*, 2018, **28**, 1149–1157.

53 B. Simović, Ž. Radovanović, G. Branković and A. Dapčević, Hydrothermally synthesized  $\text{CeO}_2/\text{ZnO}$  nanocomposite photocatalysts for the enhanced degradation of Reactive Orange 16 dye, *Mater. Sci. Semicond. Process.*, 2023, **162**, 107542.

54 A. Brindha and T. Sivakumar, Visible active N, S co-doped  $\text{TiO}_2$ /graphene photocatalysts for the degradation of hazardous dyes, *J. Photochem. Photobiol. A*, 2017, **340**, 146–156.

